PHYSICS

Carbon doping of WS_2 monolayers: Bandgap reduction and p-type doping transport

Fu Zhang[1,2]*, Yanfu Lu[1]*, Daniel S. Schulman[1]*, Tianyi Zhang[1,2], Kazunori Fujisawa[2,3], Zhong Lin[2,3], Yu Lei[1], Ana Laura Elias[2,3], Saptarshi Das[2,4†], Susan B. Sinnott[1,2,5†], Mauricio Terrones[1,2,3,5†]

Chemical doping constitutes an effective route to alter the electronic, chemical, and optical properties of two-dimensional transition metal dichalcogenides (2D-TMDs). We used a plasma-assisted method to introduce carbon-hydrogen (CH) units into WS_2 monolayers. We found CH-groups to be the most stable dopant to introduce carbon into WS_2, which led to a reduction of the optical bandgap from 1.98 to 1.83 eV, as revealed by photoluminescence spectroscopy. Aberration corrected high-resolution scanning transmission electron microscopy (AC-HRSTEM) observations in conjunction with first-principle calculations confirm that CH-groups incorporate into S vacancies within WS_2. According to our electronic transport measurements, undoped WS_2 exhibits a unipolar n-type conduction. Nevertheless, the CH-WS_2 monolayers show the emergence of a p-branch and gradually become entirely p-type, as the carbon doping level increases. Therefore, CH-groups embedded into the WS_2 lattice tailor its electronic and optical characteristics. This route could be used to dope other 2D-TMDs for more efficient electronic devices.

INTRODUCTION

Semiconducting transition metal dichalcogenides (TMDs) are an emerging group of atomically thin two-dimensional (2D) materials having attractive electronic (1), magnetic (2), and optical properties (3). A lot of research has been directed to the exploration of their applications for tunable electronics and catalysts. Unlike other engineering methods such as chemical functionalization (4), which mainly relies on the electron transfer between TMDs and adsorbed organic species, substitutional doping is able to controllably tailor both the material's bandgap and crystalline structure, as demonstrated theoretically (5) and experimentally (6, 7). The tunable bandgaps can excite cutoff detection wavelengths in a wide range including both the visible light and near-infrared regions, which makes doped TMDs suitable for applications in optoelectronics, such as photo-sensors (7). New functionalities, including emerging spin-orbit anisotropies, thermal transport anisotropies (8), and the rising of magnetic order (9), have also been explored for doped TMDs. The approach used to dope TMDs is highly dependent on the elements that could be introduced into the crystalline lattice. For example, niobium and tantalum can substitute the metal cation in TMDs to achieve a p-type electronic behavior (10, 11). In addition, chalcogen doping could achieve stable and controllable tailoring of TMDs. A p-type doping behavior can also be obtained or enhanced by introducing substitutional phosphorus in MoS_2-based field-effect transistors (FETs) (12), as well as through oxygen molecule physisorption (13). In a recent report, covalent nitrogen doping resulted in variations of the MoS_2 electronic structure (14).

Carbon has been commonly used as an acceptor anion dopant for bulk semiconductors such as GaAs (15) and its alloys (e.g., AlGaAs and InGaAs) (16), using liquid carbon tetrachloride (CCl_4) as a source, due to its low activation energy, low diffusivity, high solid solubility, and attractive electrical and optical properties. Previous work has been reported on the incorporation of carbon into several TMDs. For example, rather severe reactions between carbon precursors and MoS_2 have been reported by high-temperature (or long period) treatments of MoS_2 in a carbon-rich environment [C_2H_2 (17) or degreasing cotton (18)]. Those reported mixed phases of TMDs and transition metal carbides can be used for electro- or photocatalysis applications (17, 18). On the other hand, MoS_2 can be directly converted into molybdenum carbide via high-temperature annealing in a methane environment, thus providing a low resistance and small Schottky barrier height for the Mo_2C/MoS_2 hybrid structures (19). Theoretical simulations have predicted that tunability of the electronic structure of the MoS_2 can be achieved through substitutional carbon doping, which will have a profound effect on their optical and electronic properties (20, 21).

In this study, we demonstrate a plasma-assisted strategy to incorporate carbon species as substitutional dopants within the lattice of WS_2 monolayers, which leads to significant changes in the optical bandgap and progressively transforms the electronic transport characteristics of WS_2 monolayers. In this context, plasma treatments have been demonstrated as an efficient way to incorporate foreign atoms, such as hydrogen (22, 23), nitrogen (14), fluorine (24), and phosphorus (12) in MoS_2, via anion substitutional doping. On the basis of that strategy, we have now developed a plasma-assisted approach to effectively introduce substitutional carbon atoms within WS_2 monolayers. These carbon-doped WS_2 monolayers exhibit tunable optical and electronic properties, as revealed by both experimental measurements and theoretical simulations. In addition, first-principle calculations also indicate the most energetically

[1]Department of Materials Science and Engineering, The Pennsylvania State University, University Park, PA 16802, USA. [2]Center for Two-Dimensional and Layered Materials, The Pennsylvania State University, University Park, PA 16802, USA. [3]Department of Physics, The Pennsylvania State University, University Park, PA 16802, USA. [4]Department of Engineering Science and Mechanics, The Pennsylvania State University, University Park, PA 16802, USA. [5]Department of Chemistry, The Pennsylvania State University, University Park, PA 16802, USA.
*These authors contributed equally to this work.
†Corresponding author. Email: mut11@psu.edu (M.T.); sbs5563@psu.edu (S.B.S.); sud70@psu.edu (S.D.)

favorable configurations of carbon-hydrogen species present within the WS_2 lattice, along with their corresponding contribution to the electronic structure of the system. Aberration-corrected high-resolution scanning transmission electron microscopy (STEM) (AC-HRSTEM) is used to identify the presence of substitutional carbon within the WS_2 lattice. Electrical characterization of these doped TMD layers confirm that carbon can act as a p-type dopant in WS_2.

RESULTS

Monolayers of WS_2 were synthesized by atmospheric pressure chemical vapor deposition (CVD) using precursors in a powder form (see Materials and Methods for details). Carbon doping (schematically shown in Fig. 1A) was achieved through an inductively coupled plasma-enhanced CVD (PECVD) process, in which the plasma was generated by radio frequency (13.56 MHz) at a power of 50 to 70 W. The dopant precursor used was methane (CH_4), and the carrier gas was a mixture of Ar/H_2 (85%/15%). There is no significant structural degradation of the WS_2 samples after the PECVD process, as demonstrated by a representative scanning electron microscopy (SEM) micrograph depicted in Fig. 1B. Control experiments in which the pristine WS_2 samples were heated up at 400°C with or without the presence of Ar/H_2 plasma (in the absence of CH_4) were also carried out, and those samples were studied and compared against the synthesized carbon-doped WS_2. The advantage of the plasma-assisted route is that it leads to the decomposition of CH_4 into reactive radicals (possibly carbon and hydrocarbons) at a temperature much lower than the decomposition temperature (14, 21, 22, 25).

The optical properties of pristine (undoped) and carbon-doped WS_2 monolayers were studied by photoluminescence (PL) and Raman spectroscopies (Fig. 1, C and D). For pristine monolayers of WS_2, a single PL peak at 1.98 eV was detected [corresponding to the A exciton (26); see Fig. 1C]. PL spectra of control pristine samples heat-treated at 400°C under an Ar/H_2 atmosphere (in the absence of plasma) were obtained, and the spectra were similar to that of pris-

tine WS_2, with a slight decrease in intensity (see fig. S1). When WS_2 was treated only with Ar/H_2 plasma at 400°C, a slight red shift in the PL was observed, and the PL intensity decreased significantly (fig. S1). This decrease in the PL constitutes an indirect evidence of the presence of defects (such as sulfur vacancies) within the WS_2 lattice caused by the plasma bombardment, which could assist carbon doping. WS_2 samples treated with plasma with a different CH_4 flow (2, 3.5, and 5 sccm; Ar/H_2 as carrier gas at a flow of 100 sccm) exhibit significant changes in their PL spectra, as seen in Fig. 1C. The PL intensity decreased progressively as the CH_4 gas flow increased. Moreover, the PL peak shifted progressively toward lower energy values, and it broadened as new emissions were detected. For the WS_2 sample treated under a CH_4 flow of 5 sccm, the center of the PL emission was located at 1.83 eV, which represents a shift of 150 meV, when compared to the pristine WS_2. Note that the enhancement of full width at half maximum of PL spectra observed after introducing carbon atoms is possibly due to the generation of additional sulfur vacancies and more random doping of carbon-hydrogen units within WS_2 during the PECVD process. The uniformity of the modulated PL emission was probed by PL mappings, which show a uniform intensity throughout the carbon-doped WS_2 monolayer (see fig. S2, A and B).

Representative Raman spectra of the pristine and carbon-doped samples are shown in Fig. 1D. Besides the two first-order characteristic Raman signatures of pristine WS_2 monolayers, the E′(Γ) and A$_1$′(Γ) located at 355 and 417 cm^{-1}, respectively, a high-intensity second-order double-resonance peak involving two longitudinal acoustic phonons [2LA(M) mode] was detected when exciting the samples with a 514-nm laser (27). Such a double-resonance process was progressively suppressed when increasing the CH_4 flow, as observed in the spectra obtained from all the carbon-doped samples (see Fig. 1D). We believe that carbon dopants induced changes in the WS_2 electronic structure, which drive the system out of resonance for both the electron-phonon– and hole-phonon–mediated processes (27). In particular, one LA phonon and one defect elastic scattering are
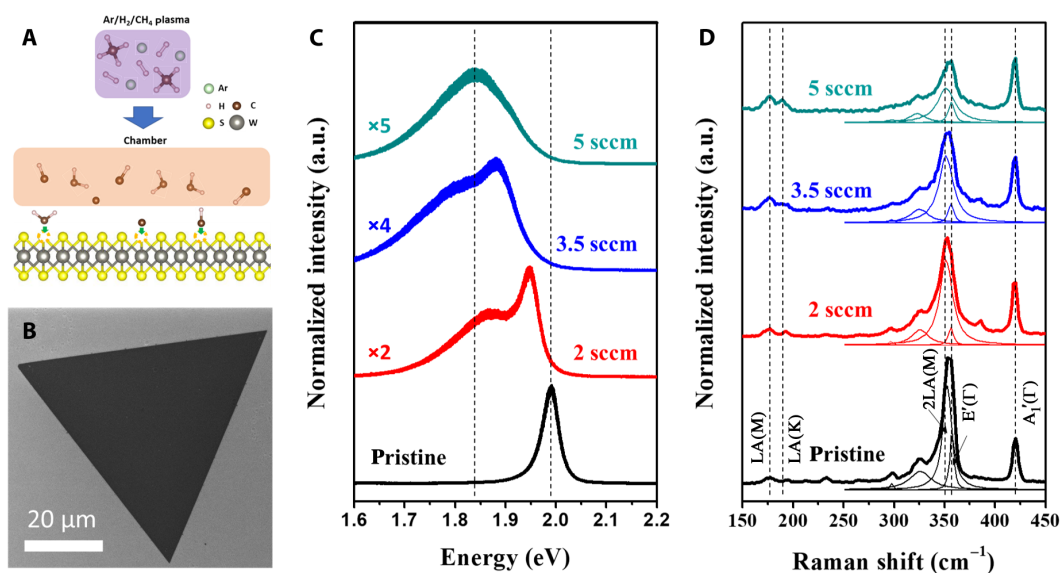
Fig. 1. Doping schematics and optical properties. (**A**) Schematics of the plasma-assisted doping experiment. (**B**) SEM image of the carbon-doped monolayer WS_2. (**C**) PL and (**D**) Raman spectra of the undoped and carbon-doped monolayered WS_2 islands, with different methane flow rates during the plasma treatment (2, 3.5, and 5 sccm, respectively) obtained with a laser excitation of 488 and 514 nm, respectively. a.u., normalized Raman intensity shown in arbitrary units.

involved in the double resonance process that give rise to the LA(M) and the LA(K) modes at 176 and 188 cm^{-1}, respectively (28). Both defect-activated modes are present in the doped samples, which provides further evidence of lattice deformation induced by either vacancies or dopants (28). It is noteworthy that samples treated in the presence of 8 sccm of CH_4 (the highest flow used in this study) preserve the characteristic Raman signature of WS_2 and exhibit the highest intensity for the LA(M) and LA(K) bands among all the samples. Moreover, the PL on this heavily doped sample is quenched (fig. S2, C and D).

The chemical bonding environment of carbon in monolayer WS_2 was also investigated by x-ray photoelectron spectroscopy (XPS; see fig. S3). Survey scans and high-resolution C1s and W4f spectra were obtained from pristine and carbon-doped WS_2 monolayers. The high-resolution scans were used to estimate the total atomic percentage of carbon in the samples, and it was found to increase from 1.98 atomic % (at %) to c.a. 5.33 at % for the carbon-doped WS_2 sample (@ 5 sccm, defined as plasma treated at methane flow rate of 5 sccm). Assuming that undoped WS_2 has only adventitious carbon, we estimate the carbon atomic percentage incorporated in the WS_2 sample to be c.a. 3.3 at %. As the carbon content of the doped samples increases, we also observe a reduction in both the oxygen content and sulfur/tungsten ratio (composition table is shown in fig. S3). The carbon incorporation also reduces the energy of the valence band maximum (VBM) to the Fermi level, as indicated in fig. S4. The red shifts in the A excitonic transition observed in the ultraviolet-visible (UV-vis) spectra (fig. S5) further support the bandgap reduction due to carbon doping.

Density functional theory (DFT) calculations were performed to further investigate the bonding environment of the carbon dopants, the associated electronic structure of the carbon-doped WS_2 systems, and the mechanism responsible for the changes observed in the optical bandgap. Besides the plasma-induced defects, CVD-grown pristine WS_2 samples can naturally have sulfur monovacancies (V_S) and divacancies (V_{S2}) (29). To introduce carbon in WS_2 monolayers, we removed S atoms from the WS_2 surface to make the V_S concen-

tration 2.67 at % in the lattice. Since the defect concentration associated with divacancies (V_{S2}) and trivacancies [removal of one metal atom and three adjacent sulfur atoms (V_{WS3})] has been documented to be much lower than that of single sulfur vacancies (V_S) (30), we only considered the V_S case for our DFT calculations. Assuming that carbon and hydrocarbon radicals are present during the WS_2 plasma treatment, carbon atoms, CH or CH_2 molecules are introduced into the WS_2 in the V_S positions. The first set of DFT calculations compared the doped WS_2 while varying the horizontal location of carbon dopants against the total energy of the pristine WS_2. When the carbon dopants ($-CH_2$) in WS_2 were at least 7.5 Å away from each other, the calculated energy difference compared to that of pristine WS_2 increased by 0.090 eV/atom, which we define as cohesive energy. When two carbon atoms were second nearest neighbors, the cohesive energy increased by 0.100 eV/atom. Such a low energy difference leads to the conclusion that there is no coupling between two carbon atoms within the WS_2 lattice, and our theoretical calculations do not reflect a tendency to carbon atom aggregation.

To verify the most stable vertical location of the carbon species within the WS_2 lattice, three separate models were built, as depicted in Fig. 2, which correspond to placing the carbon at the sulfur position (α position), placing it at the preferred W—C bond length in bulk tungsten carbide of 2.12 Å (γ position) and placing the carbon at a vertical location that is intermediate between α and γ (β position). All the proposed structures were allowed to relax, and the position of the carbon-hydrogen species did not significantly change after relaxation (less than 0.02 Å). The electronic configuration of the carbon dopants may vary considerably from a single carbon atom, a −CH group, or a −CH_2 group. The cohesive energy of the systems for each type of carbon dopant in every vertical position (α, β, or γ) is provided in Table 1. Our results indicate that the lowest cohesive energy results when the CH species are located in the β position of the WS_2 followed closely by WS_2 with CH_2 species introduced in the α and β positions. Therefore, our calculations predict that single carbon atoms are not the most stable form of carbon doping for this TMD system.
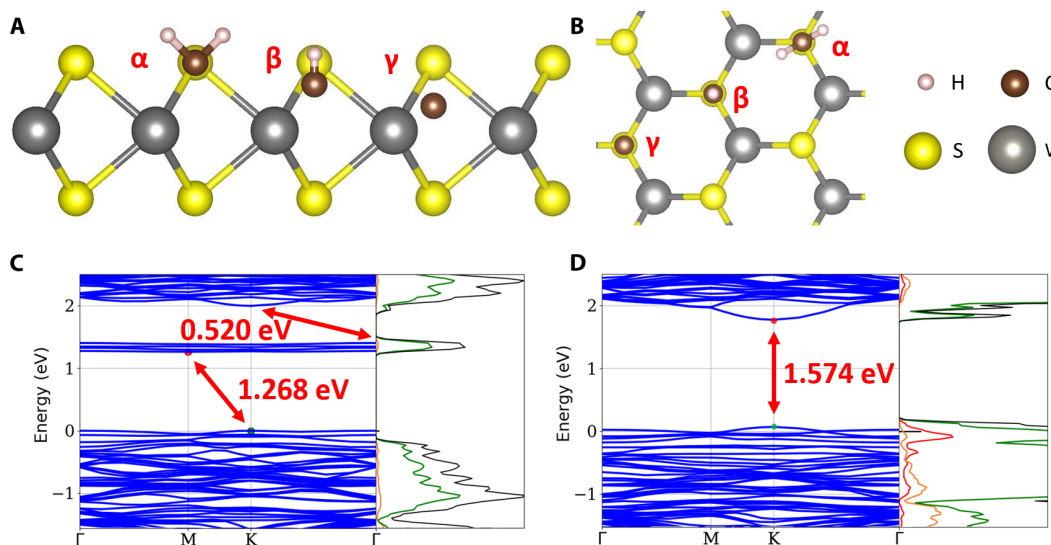
Fig. 2. Simulations of possible doping positions and band structures. Side (**A**) and top (**B**) views of α, β, and γ doping positions for the proposed carbon species: C, CH, and CH_2. (**C** and **D**) Band structure and DOS of (C) WS_2 with 2.67 at % monovacancies and (D) CH-doped WS_2 with the dopant at the β position. In the DOS, the p orbitals of the carbon atom and the tungsten atom, the d orbital of the tungsten atom, and total DOS are illustrated in different colors.

**Table 1. Relative cohesive energies of defective, doped WS$_2$ systems.** The reference cohesive energy state is that of the pristine WS$_2$, and the α, β, and γ doping positions for the proposed carbon species (C, CH, and CH$_2$) are schematically shown in Fig. 2.

Premade vacancy type	Type of doping group	Cohesive energy comparison (eV/atom)		
		Doped C position		
		α	β	γ
Monovacancy	C	0.185	0.124	0.134
	CH	0.119	0.088	0.146
	CH$_2$	0.090	0.090	0.196

In addition, we calculated the local strain at the dopant locations, which was found to be the smallest for CH-doped WS$_2$ (table S1).

The calculated bandgap of pristine WS$_2$ was 1.791 eV, as obtained using the local density approximation (LDA), which is well known to underestimate the bandgap in semiconductors (fig. S6A). The calculated band structure of the WS$_2$ with monovacancies is illustrated in Fig. 2C, which indicates that an intermediate energy state was formed at 0.520 eV below the conduction band. Thus, V$_S$ behaves like an n-type dopant in agreement with a previous report (*31*). Figure 2D exhibits the band structure of carbon-doped WS$_2$ with the CH dopant occupying the β position. Carbon-doped WS$_2$ was predicted to have a direct bandgap in which the energy decreased by 0.217 eV relative to pristine WS$_2$. Moreover, the density of states (DOS) further indicates that the acceptor level rose above the original valence band for carbon-doped WS$_2$, so that extra holes moved up to higher energy levels, thus shrinking the bandgap. In this instance, the doping group CH acted as a p-type dopant. The d orbital of W and p orbital of C dominated the contribution of the energy level of the top valence band, indicating an emerging bond between W and C to be the main reason for the bandgap reduction. The DOS of the other two cases with low cohesive energy (CH$_2$@α and CH$_2$@β) are depicted in fig. S6 (B and C). Conversely, the donor level descended below the original conduction band so the doping atoms acted as n-type dopants. On the basis of the DOS, the intermediate state emerged primarily from the d orbital of the W atom. H atoms provide more electrons to the carbon when the carbon atom is located on the surface (α position). Since a scattered doping configuration is predicted to be more stable than an aggregated doping configuration, we expect carbon to be incorporated within the WS$_2$ lattice without the carbide formation at the WS$_2$ surface. This was further experimentally confirmed by using several techniques, as will be described below.

High-angle annular dark-field (ADF) (HAADF)–STEM imaging was used to confirm the presence of carbon dopants at the V$_S$ sites (shown in Fig. 3 and fig. S7). The experimental atomic-resolution HAADF-STEM image of a carbon-doped WS$_2$ monolayer [shown in large area in Fig. 3A, V$_S$ in Fig. 3D, and carbon doping (@ 5 sccm) in Fig. 3E] reveals the existence of V$_S$ in the hexagonal lattice due to the growth process and/or postgrowth plasma treatment. A portion of sulfur monovacancies were occupied by one CH unit (CH@V$_S$, consistent with simulations). According to our STEM simulations, a slight yet clear intensity contrast difference can be generated after a CH unit occupies a V$_S$ because of the *Z*-contrast imaging mechanism of STEM (*32*) (Fig. 3, F to H; see also simulation details in Materials and Methods). The intensity profiles in Fig. 3 (B and C) and
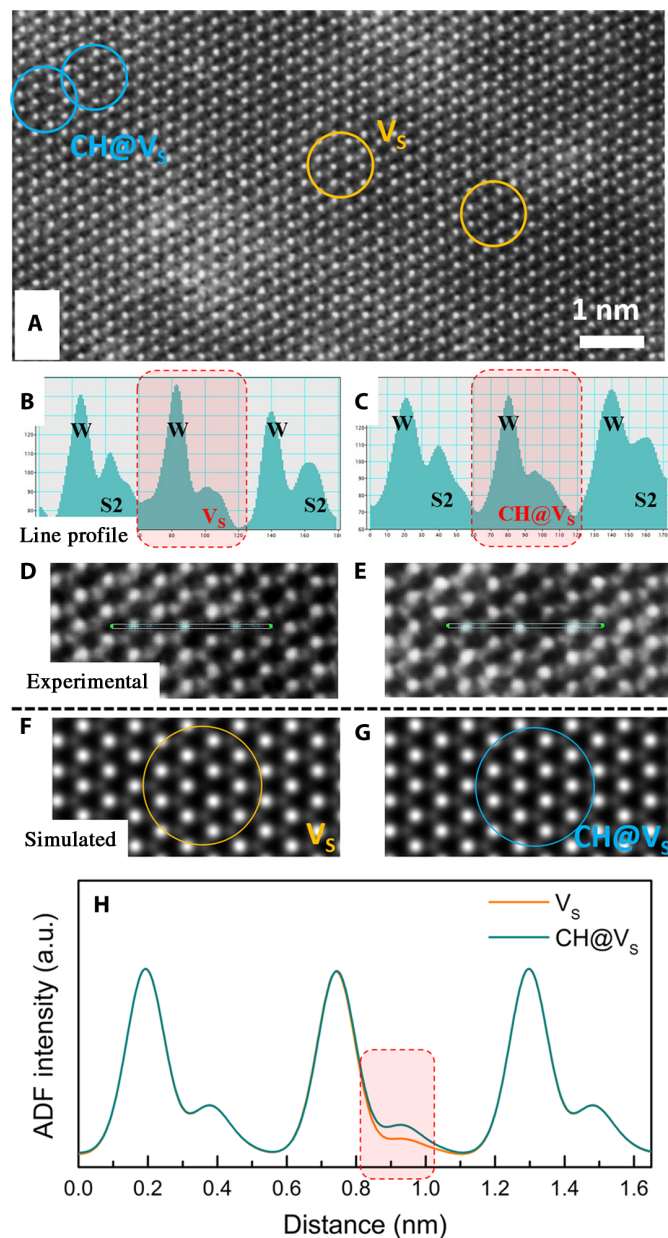
Fig. 3. TEM evidence of carbon doping in WS$_2$. Comparison between simulated and experimental HAADF-STEM images (the case of sulfur vacancies and a CH dopant occupying a sulfur vacancy) is shown. Experimental atomic-resolution HAADF-STEM image of the carbon-doped monolayer WS$_2$ (**A**) shows an area with both sulfur vacancies (V$_S$; yellow circles) and the CH dopant occupied sulfur monovacancies (CH@V$_S$; blue circles) in the carbon-doped monolayer WS$_2$. (**B**) and (**D**) show a sulfur monovacancy and its corresponding intensity line profiles, and (**C**) and (**E**) show the CH@V$_S$ and its corresponding intensity line profiles. (**F** and **G**) Simulated HAADF-STEM image of the carbon-doped monolayer WS$_2$ with (F) V$_S$ and (G) a CH@V$_S$ in the hexagonal lattice. (**H**) Intensity line profile of the STEM image simulations with V$_S$ and CH@V$_S$ in the doped monolayer WS$_2$.

fig. S7 depict the contrast difference between the V$_S$ and CH@V$_S$ and are in good agreement with simulations. As the samples were transferred using a polymer film as a support layer, some areas had contamination, and the intensity profile line scan and analyses avoid the contaminated polymer residue regions (which can be easily distinguished
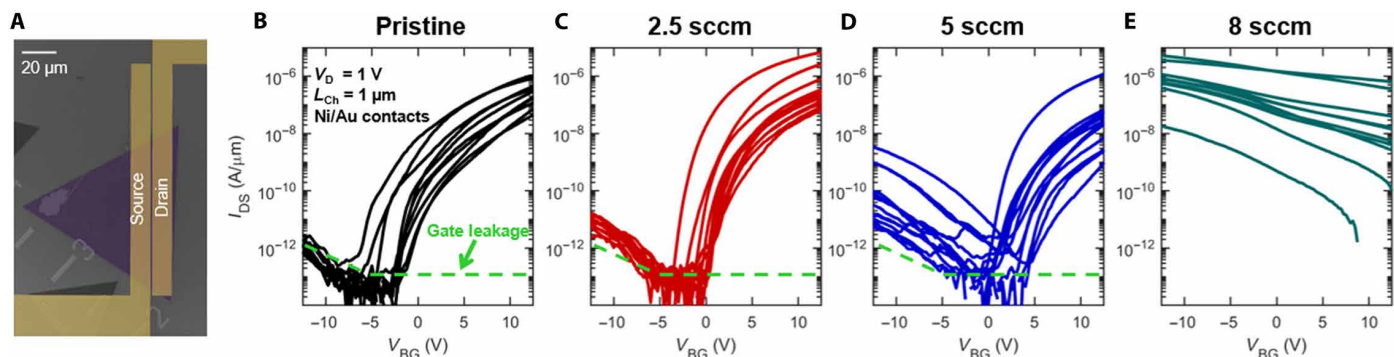
Fig. 4. FET characteristics of pristine and carbon-doped monolayer WS₂. (**A**) False-colored SEM image of a representative FET with a channel length (L_{Ch}) of 1 μm with 40-nm Ni/30-nm Au contacts on a 50-nm atomic layer deposition (ALD) Al_2O_3/Pt/TiN/Si substrate. (**B** to **E**) Drain voltage (I_{DS}) versus back gate voltage (V_{BG}) with a drain voltage (V_D) of 1 V for FETs fabricated with (B) pristine, (C) lightly doped (2.5 sccm), (D) medium-doped (5 sccm), and (E) heavily doped (8 sccm) WS₂, respectively. Each curve corresponds to a different device. The green dashed line indicates the gate leakage current level, and any drain current below this level is not the true I_{DS}. The pristine, lightly, and medium-doped samples (B to D) are primarily n type, indicating that the contact Fermi level pinning is preventing hole injection into the channel. The medium-doped samples (D) begin to show some ambipolar p-type conduction. The heavily doped device (E) reveals p-type behavior and enhanced hole injection from the contacts.

from the background) to preserve atomic cleanness of the selected experimental image areas. When comparing these experimental images and our STEM image calculation results (Fig. 3H), there is a slight difference in the intensity (for both W and S) that originates from aberrations and astigmatism in TEM; such mismatch between STEM simulation and experimental direct measurements is inherent to the thermal and beam-induced vibration of the atoms, and it is therefore unavoidable.

Pristine and WS₂ monolayers with varying levels of carbon doping treated under CH₄ flows of 2.5, 5, and 8 sccm, i.e., lightly, medium, and heavily doped, respectively, were integrated in back-gated FETs to investigate their transport characteristics. Figure 4A depicts a SEM image of a FET device, with a 50-nm Al_2O_3 gate dielectric, a channel length of 1 μm, and a channel width equal to the width of the triangular flake (~50 to 100 μm). Drain currents (I_{DS}) versus back gate voltages (V_{BG}) at a drain voltage (V_{DS}) of 1 V are shown in Fig. 4 (B to E) for all 10 pristine, 13 lightly doped, 13 medium-doped, and 10 heavily doped WS₂ devices, respectively. The mobility cannot properly be extracted since most of the devices do not consistently reach the full ON state, i.e., there is no linear region of the I_{DS} versus V_{BG}. However, the electron mobility is estimated to be between ~0.1 and 1 cm²/V•s from the few that exhibit a linear behavior.

The pristine WS₂ devices exhibited unipolar n-type behavior with an ON/OFF ratio of >10⁶ for the n-branch ($V_{BG} > 0$), indicating that the metal Fermi level (E_F) pins closer to the WS₂ conduction band (E_C) than the valence band (E_V), thus resulting in a smaller electron Schottky barrier height (Φ_{SB-n}) than hole Schottky barrier height (Φ_{SB-p}) (*33*). Note that green dashed lines in Fig. 4 (B to E) denote the approximate gate leakage current. For the pristine samples in Fig. 4B, the current seen at $V_{BG} < -5$ is not the true device current and thus is not an indication of hole conduction. However, a low current p-branch corresponding to hole conduction begins to emerge as the carbon doping is gradually introduced, as observed in the lightly and medium-doped devices shown in Fig. 4 (C and D, respectively). For the medium-doped samples shown in Fig. 4D, significant device-to-device variation (due to variation of plasma power) is observed, but many devices have nearly symmetric n- and p-branches. The ambipolar characteristics thus indicate that as the degree of doping increases, the tunnel barrier height for the holes, and thus Φ_{SB-p}, decreases, as

shown schematically in fig. S8. This arises from one or a combination of two mechanisms. The sum of the electron and hole Schottky barriers equals the bandgap ($\Phi_{SB-n} + \Phi_{SB-p} = E_G$). As E_G decreases, either Φ_{SB-n}, Φ_{SB-p}, or both can decrease. Moreover, the energy level at which the metal Fermi level pins relative to the WS₂ conduction and valence band can change. For a given E_G, a decrease in Φ_{SB-p} will accompany an increase in Φ_{SB-n} and a reduction in the n-branch current. The emergence of the p-branch when comparing the pristine, lightly doped, and medium-doped devices is difficult to attribute to either single mechanism. Any changes in Φ_{SB-n} that affect the n-branch ON current are easily obscured upon variation in the subthreshold slope (SS), which is heavily affected by the interface quality and, potentially, the doping procedure.

The heavily carbon-doped devices exhibit an entirely p-type current when compared to lower-doped samples. At $V_{BG} = 0$ V, the devices are now in the ON state since the doping has now pushed the Fermi level close to the valence band. This heavy doping accompanied by the realignment of the metal-WS₂ Fermi level pinning results in a significantly decreased Φ_{SB-p}. The hole injection is no longer blocked by a large Schottky tunnel barrier. This is evident in the linear I_{DS} versus V_{DS} characteristics shown in fig. S9. Although the currents are relatively large, ~1 μA/μm, at $V_{BG} = -12$ V, the device cannot be turned off at positive V_{BG}. This indicates that the CH₄ plasma treatment using the 8 sccm CH₄ flow rate decreased the WS₂/Al_2O_3 coupling, slowing the band movement because of the creation of interface trap states. This degradation only appears at the highest doping level. The samples treated with the 2.5 sccm CH₄ flow rate have shown an improved SS when compared to the pristine samples, possibly due to an annealing effect occurring during the 400°C doping treatment. A true post-growth substitutional doping scheme such as the novel carbon doping route presented here is required to achieve n+/p/n+ and p+/n/p+ doping profiles required for CMOS circuits. A traditional surface electrostatic doping approach would be insufficient.

DISCUSSION

In this study, we have successfully incorporated carbon-hydrogen groups within sulfur monovacancies of WS₂ following a novel plasma-assisted approach. This two-step strategy does not involve high

temperatures for the doping step (only 400°C). Moreover, we have demonstrated that the carbon-doped monolayers of WS_2 exhibit optical and electronic properties that could be tuned depending on the carbon content. The PL measurements indicated that the bandgap could be reduced by 150 meV, when compared to that of the pristine WS_2 monolayer. In addition, AC-HRSTEM imaging and DFT calculations confirmed the presence of covalently bonded carbon-hydrogen groups within the WS_2 lattice. Furthermore, we performed a detailed electrical characterization, which indicates that the carbon-hydrogen groups within WS_2 lead to a p-type doping conductor. Complementary metal-oxide semiconductor (CMOS) devices are engineered to be unipolar and require n- and p-type carrier transport for the N-MOS (n-type MOS) and P-MOS (p-type MOS) transistors using n+/p/n+ and p+/n/p+ substitutional doping schemes, respectively. Therefore, the demonstrated substitutional p-doping presented here constitutes a significant step toward CMOS logic circuits based on TMD materials. In summary, we have identified novel structure-property correlations and compositional recipes for designing 2D TMD-based materials, which will have a significant impact for novel applications, especially energy-efficient photo-electric devices and FET devices.

MATERIALS AND METHODS

Atmospheric pressure CVD synthesis of monolayer WS_2

Pristine monolayer WS_2 samples were synthesized by atmospheric pressure CVD (34). A quartz tube furnace with ultrahigh purity argon as the carrier gas was used as the reaction chamber. Mixed powders of WO_3 and NaBr (5 mg:1 mg) were loaded inside an aluminum boat, and air plasma–cleaned Si/SiO_2 wafers were placed on top of the boat facing down. Sulfur powders (300 mg) were located upstream and were vaporized at 250°C during the experiments. In a typical 15-min synthesis, WO_3 and NaBr powders along with the growth substrate were heated up to 825°C, while the sulfur was simultaneously heated up by a heating tape. The furnace was allowed to cool to room temperature naturally.

Plasma-assisted carbon doping of monolayer WS_2

As-grown WS_2 monolayers were placed at the hot zone of a home-built inductively coupled PECVD system. The plasma was generated by applying radio frequency (13.56 MHz) to a mixture of CH_4 and Ar/H_2. At around 1 torr, the system was ramped up to 400°C in 15 min, and the experiment was carried out for 10 min. The flow of Ar/H_2 was 200 sccm during the treatment, and the flow of CH_4 varied from 2 to 8 sccm, to achieve samples with various doping levels. It is noteworthy that the decision of using methane (CH_4) over ethane (C_2H_6), ethylene (C_2H_4), acetylene (C_2H_2), or other hydrocarbons is due to the simplification of the active hydrocarbon plasma species present in the chamber only to CH_x-, which act as anion substitutions for S within the WS_2 lattice. The other listed options for hydrocarbon gases may generate plasma species containing more than one carbon atom, which would have complicated the kinetics of the process and our DFT modeling.

Materials characterization

SEM was carried out using a Zeiss Merlin field-emission scanning electron microscope at an accelerating voltage of 5 kV. A Renishaw inVia microscope with a Coherent Innova 70C argon-krypton laser with photon wavelengths of 488 and 514 nm was used for acquiring the Raman and PL spectra using a backscattering configuration with a grating (1800 line/mm). XPS experiments were performed using a Physical Electronics VersaProbe II instrument with monochromated Al-Kα x-ray source. The binding energy axis was calibrated using sputter-cleaned Cu foil (Cu $2p_{3/2}$ = 932.7 eV and Cu $2p_{3/2}$ = 75.1 eV). Peaks were charge referenced to the CH_x band in the C 1s spectra at 284.8 eV. Measurements were made at a takeoff angle of 45° with respect to the sample surface plane. Atomic quantification was performed using instrumental relative sensitivity factors that account for the x-ray cross section and inelastic mean free path of the electrons. Aberration-corrected STEM imaging and microscopy were performed with a FEI Titan[3] G2 60-300 microscope, operated at 80 kV with double spherical aberration correction, offering subangstrom imaging resolution. A HAADF detector with a collection angle of 42 to 244 mrad, a camera length of 115 mm, a beam current of 45 pA, and a beam convergence of 30 mrad was used for STEM image acquisition. For the HAADF-STEM images, a Gaussian blur filter (r = 2.00) was applied (ImageJ program) to eliminate noise and enhance the visibility of structural details, while the line profiles of ADF intensity were captured by analyzing the raw STEM images.

STEM simulations

Atomic-resolution STEM image simulations were conducted by using the QSTEM package (35). The applied parameters, acceleration voltage, convergence angle and inner/outer angle for the HAADF detector, and spherical aberration (C_3 and C_5) were all adjusted according to the experimental conditions.

DFT calculations

Before building the whole supercell, the monolayer of WS_2 was fully relaxed so that it could reach the minimum energy state. To construct a model with an appropriate concentration of vacancies or dopants, the three-atom model was expanded to a 5×5 supercell horizontally. The DFT calculations used the plane-wave basis and projector augmented wave (PAW) method (36) within the Vienna Ab initio Simulation Package (37). Convergence tests indicate that energies were converged to within 1 meV/atom with a 680-eV cutoff energy, 20 Å of vacuum in the direction perpendicular to the interface, and a $13 \times 13 \times 1$ k-point mesh. In the study of vertical position of carbon-hydrogen species within the WS_2, separate models were built because only three local energy minimum states were found corresponding to the α, β, and γ positions. To monitor the local energy minimum states, carbon-hydrogen species were not moved over 0.15 Å compared to their initial positions during the relaxation of each calculation when each possible position was at least 0.3 Å apart. Band structure calculations were performed using the LDA (38). This choice of functional was used because the calculated bandgap of pure WS_2 using LDA was 1.791 eV, as shown in fig. S6, which is closer to the PL measurement than the results obtained using the generalized gradient approximation (39) and hybrid functional (40). Although the LDA underestimates the bandgap in semiconductors and insulators compared with experimental results, the results are reasonably accurate since the inaccuracy comes from systematic error instead of any physical error. The band structure and DOS also revealed the change of each band, each orbital of elements, and types of doping.

Device fabrication and test

The back-gated WS_2 FETs were fabricated by first transferring the undoped and carbon-doped WS_2 from the growth substrate onto a

Si p^{++}/TiN/Pt substrate with a 50-nm Al_2O_3 gate dielectric grown via ALD using a poly(methyl methacrylate) (PMMA)–assisted transfer process. The source and drain regions were patterned using electron beam lithography with a bilayer copolymer PMMA process and developed in a 1:1 methyl isobutyl ketone: isopropyl alcohol (IPA) solution. Electron beam evaporation was used to deposit the 40-nm Ni/30-nm Au contacts, followed by a lift-off procedure in acetone and IPA. The devices were measured after sitting in high vacuum ($<10^{-5}$ torr) for >8 hours to eliminate any transient effects due to adsorbed species.

SUPPLEMENTARY MATERIALS

Supplementary material for this article is available at http://advances.sciencemag.org/cgi/content/full/5/5/eaav5003/DC1

Fig. S1. PL responses of reference samples.
Fig. S2. PL mapping of carbon-doped WS_2, Raman and PL of heavily carbon-doped WS_2.
Fig. S3. XPS analyses of the carbon-doped WS_2.
Fig. S4. VBM spectra of the carbon-doped WS_2.
Fig. S5. UV-vis spectra of the carbon-doped WS_2.
Fig. S6. Complementary band structures and DOS of monolayer pristine WS_2 and carbon-doped WS_2.
Fig. S7. Experimental STEM examples and identification of sulfur monovacancies and carbon dopant in pristine and carbon-doped WS_2 monolayers.
Fig. S8. Band diagram showing the change in Fermi level pinning.
Fig. S9. Transfer and output characteristics of a carbon-doped WS_2–based FET (@8 sccm CH_4).
Table S1. Local strain of WS_2 with premade single vacancies and different ligands on C atoms and dopant positions.

REFERENCES AND NOTES

1. Q. H. Wang, K. Kalantar-Zadeh, A. Kis, J. N. Coleman, M. S. Strano, Electronics and optoelectronics of two-dimensional transition metal dichalcogenides. *Nat. Nanotechnol.* **7**, 699–712 (2012).
2. Y. Ma, Y. Dai, M. Guo, C. Niu, J. Lu, B. Huang, Electronic and magnetic properties of perfect, vacancy-doped, and nonmetal adsorbed $MoSe_2$, $MoTe_2$ and WS_2 monolayers. *Phys. Chem. Chem. Phys.* **13**, 15546–15553 (2011).
3. F. H. L. Koppens, T. Mueller, Ph. Avouris, A. C. Ferrari, M. S. Vitiello, M. Polini, Photodetectors based on graphene, other two-dimensional materials and hybrid systems. *Nat. Nanotechnol.* **9**, 780–793 (2014).
4. T. S. Sreeprasad, P. Nguyen, N. Kim, V. Berry, Controlled, defect-guided, metal-nanoparticle incorporation onto MoS_2 via chemical and microwave routes: Electrical, thermal, and structural properties. *Nano Lett.* **13**, 4434–4441 (2013).
5. H.-P. Komsa, A. V. Krasheninnikov, Two-dimensional transition metal dichalcogenide alloys: Stability and electronic properties. *J. Phys. Chem. Lett.* **3**, 3652–3656 (2012).
6. J. Kang, S. Tongay, J. Li, J. Wu, Monolayer semiconducting transition metal dichalcogenide alloys: Stability and band bowing. *J. Appl. Phys.* **113**, 143703 (2013).
7. V. Klee, E. Preciado, D. Barroso, A. E. Nguyen, C. Lee, K. J. Erickson, M. Triplett, B. Davis, I.-H. Lu, S. Bobek, J. Mckinley, J. P. Martinez, J. Mann, A. A. Talin, L. Bartels, F. Léonard, Superlinear composition-dependent photocurrent in CVD-grown monolayer $MoS_{2(1−x)}Se_{2x}$ alloy devices. *Nano Lett.* **15**, 2612–2619 (2015).
8. A. Azizi, Y. Wang, Z. Lin, K. Wang, A. L. Elias, M. Terrones, V. H. Crespi, N. Alem, Spontaneous formation of atomically thin stripes in transition metal dichalcogenide monolayers. *Nano Lett.* **16**, 6982–6987 (2016).
9. B. Xia, P. Liu, Y. Liu, D. Gao, D. Xue, J. Ding, Re doping induced 2H-1T phase transformation and ferromagnetism in MoS_2 nanosheets. *Appl. Phys. Lett.* **113**, 013101 (2018).
10. M. R. Laskar, D. N. Nath, L. Ma, E. W. Lee II, C. H. Lee, T. Kent, Z. Yang, R. Mishra, M. A. Roldan, J.-C. Idrobo, S. T. Pantelides, S. J. Pennycook, R. C. Myers, Y. Wu, S. Rajan, p-type doping of MoS_2 thin films using Nb. *Appl. Phys. Lett.* **104**, 092104 (2014).
11. X. J. Chua, J. Luxa, A. Y. S. Eng, S. M. Tan, Z. Sofer, M. Pumera, Negative electrocatalytic effects of p-doping niobium and tantalum on MoS_2 and WS_2 for the hydrogen evolution reaction and oxygen reduction reaction. *ACS Catal.* **6**, 5724–5734 (2016).
12. A. Nipane, D. Karmakar, N. Kaushik, S. Karande, S. Lodha, Few-layer MoS_2 p-Type devices enabled by selective doping using low energy phosphorus implantation. *ACS Nano* **10**, 2128–2137 (2016).
13. S. Tongay, J. Zhou, C. Ataca, J. Liu, J. S. Kang, T. S. Matthews, L. You, J. Li, J. C. Grossman, J. Wu, Broad-range modulation of light emission in two-dimensional semiconductors by molecular physisorption gating. *Nano Lett.* **13**, 2831–2836 (2013).
14. A. Azcatl, X. Qin, A. Prakash, C. Zhang, L. Cheng, Q. Wang, N. Lu, M. J. Kim, J. Kim, K. Cho, R. Addou, C. L. Hinkle, J. Appenzeller, R. M. Wallace, Covalent nitrogen doping and compressive strain in MoS_2 by remote N_2 plasma exposure. *Nano Lett.* **16**, 5437–5443 (2016).
15. L. W. Yang, P. D. Wright, V. Eu, Z. H. Lu, A. Majerfeld, Heavily doped p-GaAs grown by low-pressure organometallic vapor phase epitaxy using liquid CCl_4. *J. Appl. Phys.* **72**, 2063–2065 (1992).
16. P. Lian, T. Yin, Z. Xu, H. Zhao, D. Zou, G. Gao, J. Du, C. Chen, C. Tao, J. Chen, G. Shen, Q. Cao, X. Ma, L. Chen, High-quality carbon-doped GaAs/AlGaAs material growth in MOCVD and its application for optoelectronic devices. *Proc. SPIE* **3547**, 10.1117/12.319617 (1998).
17. J. Wu, L. Ma, A. Samanta, M. Liu, B. Li, Y. Yang, J. Yuan, J. Zhang, Y. Gong, J. Lou, R. Vajtai, B. Yakobson, A. K. Singh, C. S. Tiwary, P. M. Ajayan, Growth of molybdenum carbide–graphene hybrids from molybdenum disulfide atomic layer template. *Adv. Mater. Interfaces* **4**, 1600866 (2017).
18. Z. Hai, J. Du, M. K. Akbari, C. Xue, H. Xu, S. Zhuiykov, Carbon-doped MoS_2 nanosheet photocatalysts for efficient degradation of methyl orange. *Ionics* **23**, 1921–1925 (2017).
19. J. Jeon, Y. Park, S. Choi, J. Lee, S. S. Lim, B. H. Lee, Y. J. Song, J. H. Cho, Y. H. Jang, S. Lee, Epitaxial synthesis of molybdenum carbide and formation of a Mo_2C/MoS_2 hybrid structure via chemical conversion of molybdenum disulfide. *ACS Nano* **12**, 338–346 (2018).
20. Q. Yue, S. Chang, S. Qin, J. Li, Functionalization of monolayer MoS_2 by substitutional doping: A first-principles study. *Phys. Lett. A* **377**, 1362–1367 (2013).
21. A.-M. Hu, L.-l. Wang, W.-Z. Xiao, G. Xiao, Q.-Y. Rong, Electronic structures and magnetic properties in nonmetallic element substituted MoS_2 monolayer. *Comp. Mater. Sci.* **107**, 72–78 (2015).
22. D. Pierucci, H. Henck, Z. Ben Aziza, C. H. Naylor, A. Balan, J. E. Rault, M. G. Silly, Y. J. Dappe, F. Bertran, P. Le Fèvre, F. Sirotti, A. T. C. Johnson, A. Ouerghi, Tunable doping in hydrogenated single layered molybdenum disulfide. *ACS Nano* **11**, 1755–1761 (2017).
23. K. Y. Ma, S. I. Yoon, A.-R. Jang, H. Y. Jeong, Y.-J. Kim, P. K. Nayak, H. S. Shin, Hydrogenation of monolayer molybdenum diselenide via hydrogen plasma treatment. *J. Mater. Chem. C* **5**, 11294–11300 (2017).
24. M. Chen, H. Nam, S. Wi, L. Ji, X. Ren, L. Bian, S. Lu, X. Liang, Stable few-layer MoS_2 rectifying diodes formed by plasma-assisted doping. *Appl. Phys. Lett.* **103**, 142110 (2013).
25. Y. Hamedani, P. Macha, T. J. Bunning, R. R. Naik, M. C. Vasudev, Plasma-Enhanced Chemical Vapor Deposition: Where we are and the Outlook for the Future, in *Chemical Vapor Deposition-Recent Advances and Applications in Optical, Solar Cells and Solid State Devices*, S. Neralla, Ed. (InTech, 2016), pp. 247–280.
26. C. Cong, J. Shang, X. Wu, B. Cao, N. Peimyoo, C. Qiu, L. Sun, T. Yu, Synthesis and optical properties of large-area single-crystalline 2D semiconductor WS_2 monolayer from chemical vapor deposition. *Adv. Opt. Mater.* **2**, 131–136 (2014).
27. A. Berkdemir, H. R. Gutiérrez, A. R. Botello-Méndez, N. Perea-López, A. L. Elías, C.-I. Chia, B. Wang, V. H. Crespi, F. López-Urías, J.-C. Charlier, H. Terrones, M. Terrones, Identification of individual and few layers of WS_2 using Raman spectroscopy. *Sci. Rep.* **3**, 1755 (2013).
28. B. R. Carvalho, Y. Wang, S. Mignuzzi, D. Roy, M. Terrones, C. Fantini, V. H. Crespi, L. M. Malard, M. A. Pimenta, Intervalley scattering by acoustic phonons in two-dimensional MoS_2 revealed by double-resonance Raman spectroscopy. *Nat. Commun.* **8**, 14670 (2017).
29. V. Carozo, Y. Wang, K. Fujisawa, B. R. Carvalho, A. McCreary, S. Feng, Z. Lin, C. Zhou, N. Perea-López, A. L. Elías, B. Kabius, V. H. Crespi, M. Terrones, Optical identification of sulfur vacancies: Bound excitons at the edges of monolayer tungsten disulfide. *Sci. Adv.* **3**, e1602813 (2017).
30. Z. Lin, B. R. Carvalho, E. Kahn, R. Lv, R. Rao, H. Terrones, M. A. Pimenta, M. Terrones, Defect engineering of two-dimensional transition metal dichalcogenides. *2D Mater.* **3**, 022002 (2016).
31. E. M. Alexeev, A. Catanzaro, O. V. Skrypka, P. K. Nayak, S. Ahn, S. Pak, J. Lee, J. I. Sohn, K. S. Novoselov, H. S. Shin, A. I. Tartakovskii, Imaging of interlayer coupling in van der Waals heterostructures using a bright-field optical microscope. *Nano Lett.* **17**, 5342–5349 (2017).
32. D. B. Williams, C. B. Carter, The Transmission Electron Microscope, in *Transmission Electron Microscopy* (Springer, 1996), pp. 3–17.
33. D. S. Schulman, A. J. Arnold, S. Das, Contact engineering for 2D materials and devices. *Chem. Soc. Rev.* **47**, 3037–3058 (2018).
34. A. L. Elías, N. Perea-López, A. Castro-Beltran, A. Berkdemir, R. Lv, S. Feng, A. D. Long, T. Hayashi, Y. A. Kim, M. Endo, H. R. Gutierrez, N. R. Pradhan, L. Balicas, T. E. Mallouk, F. Lopez-Urias, H. Terrones, M. Terrones, Controlled synthesis and transfer of large-area WS_2 sheets: From single layer to few layers. *ACS Nano* **7**, 5235–5242 (2013).
35. C. T. Koch, "*Determination of core structure periodicity and point defect density along dislocations,*" thesis, Arizona State University (2002).
36. P. E. Blöchl, Projector augmented-wave method. *Phys. Rev. B* **50**, 17953–17979 (1994).
37. G. Kresse, J. Furthmüller, Efficient iterative schemes for ab initio total-energy calculations using a plane-wave basis set. *Phys. Rev. B* **54**, 11169–11186 (1996).
38. A. Becke, Completely numerical calculations on diatomic molecules in the local-density approximation. *Phys. Rev. A* **33**, 2786–2788 (1986).
39. J. P. Perdew, K. Burke, M. Ernzerhof, Generalized gradient approximation made simple. *Phys. Rev. Lett.* **77**, 3865–3868 (1996).

40. J. Heyd, G. E. Scuseria, M. Ernzerhof, Erratum: "Hybrid functionals based on a screened Coulomb potential" [J. Chem. Phys. 118, 8207 (2003)]. *J. Chem. Phys.* **124**, 219906 (2006).

Citation: F. Zhang, Y. Lu, D. S. Schulman, T. Zhang, K. Fujisawa, Z. Lin, Y. Lei, A. L. Elias, S. Das, S. B. Sinnott, M. Terrones, Carbon doping of WS_2 monolayers: Bandgap reduction and p-type doping transport. *Sci. Adv.* **5**, eaav5003 (2019).